J. Fluid Mech. (2011), *vol.* 682, *pp.* 543–557. © Cambridge University Press 2011
doi:10.1017/jfm.2011.244

Measuring the departures from the Boussinesq approximation in Rayleigh–Bénard convection experiments

H. KURTULDU[1], K. MISCHAIKOW[2] AND M. F. SCHATZ[1]†

[1]Center for Nonlinear Science and School of Physics, Georgia Institute of Technology, Atlanta, GA 30332, USA

[2]Department of Mathematics, Rutgers University, Piscataway, NJ 08854, USA

(Received 20 August 2010; revised 10 May 2011; accepted 25 May 2011; first published online 22 July 2011)

Algebraic topology (homology) is used to characterize quantitatively non-Oberbeck–Boussinesq (NOB) effects in chaotic Rayleigh–Bénard convection patterns from laboratory experiments. For fixed parameter values, homology analysis yields a set of Betti numbers that can be assigned to hot upflow and, separately, to cold downflow in a convection pattern. An analysis of data acquired under a range of experimental conditions where NOB effects are systematically varied indicates that the difference between time-averaged Betti numbers for hot and cold flows can be used as an order parameter to measure the strength of NOB-induced pattern asymmetries. This homology-based measure not only reveals NOB effects that Fourier methods and measurements of pattern curvature fail to detect, but also permits distinguishing pattern changes caused by modified lateral boundary conditions from NOB pattern changes. These results suggest a new approach to characterizing data from either experiments or simulations where NOB effects are expected to play an important role.

Key words: Bénard convection, buoyancy-driven instability, pattern formation

1. Introduction

Convective flow plays a key role in numerous technological processes and natural phenomena, including the growth of semiconductor materials and the dynamics of the Earth's atmosphere, ocean and mantle (Getling 1998). Rayleigh–Bénard convection (RBC) of a horizontal fluid layer, confined between two thermally conducting plates, heated from below is considered a paradigm to investigate the nature of convection and has motivated numerous numerical and laboratory studies (see for example de Bruyn *et al.* 1996; Bodenschatz, Pesch & Ahlers 2000, and references therein). The exact equations governing the fluid motion in natural convection are difficult to manage. In order to simplify the equations by reducing the nonlinearity, the Oberbeck–Boussinesq (OB) approximation (Oberbeck 1879; Boussinesq 1903) is frequently used in most theoretical and numerical studies of thermal convection, including RBC. Physically, the OB approximation ignores the temperature dependence of all fluid properties, except for the temperature-induced density variation retained in the

† Email address for correspondence: michael.schatz@physics.gatech.edu

buoyant force that drives the flow. Flows observed in nature or in the laboratory never fully commit to this approximation, and non-Oberbeck–Boussinesq (NOB) effects inevitably arise. Characterizing the strength of NOB effects in observed flows could lead to the development of improved models; however, heretofore, there has been no systematic way to quantify NOB effects starting from experimental data.

We present the use of algebraic topology (computational homology) to characterize the departures from the OB approximation in RBC experiments. The homology analysis is performed on complex patterns in spatio-temporally chaotic data acquired from experiments where NOB effects are systematically varied. It is well known that solutions to the OB equations exhibit reflection symmetry about the midplane of the layer. Characterization based on homology not only reveals the breakdown of reflection symmetry but also quantifies the strength of the asymmetries. This characterization is empirical; at present, very little is understood theoretically about the algebraic topology of solutions to the governing equations for convection or for any other fluid flow. Nevertheless, as we discuss, computational homology analysis provides insight into NOB effects that other, more conventional techniques of pattern analysis fail to capture.

RBC experiments modelled by the OB approximation are described by three dimensionless quantities. The aspect ratio Γ measures the geometry of the convection cell and is defined by $\Gamma = r/d$, where r is the radius and d is the depth of a cylindrical convection cell. The Rayleigh number Ra and the Prandtl number σ that depend on the fluid properties are defined as

$$Ra = \frac{\alpha g d^3 \Delta T}{\kappa \nu}, \tag{1.1}$$

$$\sigma = \frac{\nu}{\kappa}, \tag{1.2}$$

where α is the thermal expansion coefficient, g is the acceleration of gravity, ΔT is the temperature difference between the layers, κ is the thermal diffusivity, and ν is the kinematic viscosity. As the temperature difference reaches a critical value ΔT_c ($Ra_c = 1707.8$), the destabilizing mechanism (buoyancy) overcomes the stabilizing mechanisms (heat and momentum diffusion), and the onset of convection occurs. Under Boussinesq conditions, gases exhibit straight-roll convection at onset via a supercritical bifurcation (Schluter, Lortz & Busse 1965); the convection pattern of spatial variation is composed of rolls with hot upflow and cold downflow. As the system is driven away from the onset by the control parameter (reduced Rayleigh number)

$$\epsilon = \frac{Ra - Ra_c}{Ra_c}, \tag{1.3}$$

the pattern of convective flows becomes time dependent and exhibits complex spatial structure. In particular for the $\sigma \approx 1$ case and sufficiently large ϵ we consider here, the system demonstrates a transition to the state known as spiral-defect chaos (SDC; first observed by Morris *et al.* 1993), where the convection pattern of hot and cold rolls with a spatio-temporally chaotic behaviour is deformed into rotating spirals and riddled with dislocations, disclinations and grain boundaries.

When the fluid's physical properties change little between the top and the bottom of the layer, the OB approximation describes the convective flow well; however, when the properties vary significantly over the layer depth, NOB effects should be taken into account. The departures from the OB approximation are characterized quantitatively

by the non-dimensional parameter Q introduced by Busse (1967),

$$Q = \sum_{i=0}^{4} \gamma_i \mathscr{P}_i \tag{1.4}$$

with

$$\left.\begin{aligned} \gamma_0 &= -\frac{\rho_b - \rho_t}{\rho_m}, \quad \gamma_1 = \frac{\alpha_b \rho_b - \alpha_t \rho_t}{2\alpha_m \rho_m}, \quad \gamma_2 = \frac{\nu_b - \nu_t}{\nu_m}, \\ \gamma_3 &= \frac{\lambda_b - \lambda_t}{\lambda_m}, \qquad \gamma_4 = \frac{c_{pb} - c_{pt}}{c_{pm}}, \end{aligned}\right\} \tag{1.5}$$

where ρ and c_p are density and specific heat at constant pressure, respectively, and $\lambda = \kappa \rho c_p$ is the thermal conductivity. (The subscripts b, t and m indicate fluid properties evaluated at bottom, top and mean temperature of the cell, respectively.) The coefficients $\mathscr{P}_i$ are linear functions of σ^{-1} and first given by Busse (1967) in the limit $\sigma \to \infty$. Bodenschatz *et al.* (2000) reported recalculated and corrected values of $\mathscr{P}_i$ and these coefficients were confirmed in a recent work by Ahlers *et al.* (2009). Typically, gases and liquids have positive and negative values of Q, respectively.

Strictly speaking, Q describes a specific NOB effect (hexagon-roll competition) to lowest order in γ_i; thus, the use of Q has a strong theoretical basis only in the limit of weak NOB effects (small γ_i) near convective onset ($\epsilon \ll 1$). Nevertheless, theory and experiments in strongly nonlinear regimes do use γ_i only to leading order as one way to capture NOB effects. For example, Madruga, Riecke & Pesch (2006) compute hexagonal pattern stability diagrams in the range $0 < \epsilon < 1.5$ using leading order γ_i that account for large ϵ (see § 2.1). Niemela & Sreenivasen (2003) used Q to characterize NOB effects in turbulent convection for Ra in the range 10^6–10^{15}. Our use of Q to describe NOB effects is in the same spirit: a quantity that, to date, does not yet have a firm theoretical basis in the parameter range where we use it, but, nevertheless, is related to NOB effects and is useful because it can be computed knowing only the flow's parameter values. With this limitation in mind, we show that NOB effects can be quantified in the sense that Q shows a strong empirical correlation to topological properties computed from observed flow patterns.

2. Experiments

We measure convective flow in a horizontal layer of compressed gas cooled from above and heated from below in a cylindrical convection cell (a similar apparatus is described in de Bruyn *et al.* 1996). Single-phase gases CO_2 and SF_6 are used as convective fluids, bounded by circular filter paper or plastic (polyethersulfone) lateral walls. The thermal conductivities of the paper and the plastic walls are, respectively, about a factor of 4 and 10 times larger than the thermal conductivity of the fluid used in experiments. Top and bottom temperatures are controlled within $\pm 0.02^{\circ}$C, while the pressure is controlled within ± 0.04 bar. The variation of the depth under pressure is less than 5 μm along the cell. The convective flow patterns are visualized by using the shadowgraph technique that measures variations in the vertically averaged index of refraction.

We perform experimental runs in the SDC regime under different experimental conditions in order to study the departure from the OB approximation. Key parameter values for these conditions are given in table 1. We use gaseous SF_6 in three experiments (labelled as E-I, E-III and E-IV) with a plastic lateral boundary and

Experiment	E-I	E-II	E-III	E-IV
Fluid	SF_6	CO_2	SF_6	SF_6
Boundary	Plastic	Paper	Plastic	Plastic
d (μm)	590	649	595	588
Γ	31.6	30.8	31.4	31.8
P (bar)	9.81	30.88	12.90	17.22
ΔT_c (°C)	12.37	5.49	5.01	1.70
t_v (s)	1.2	1.8	1.8	2.7
σ	0.84	0.99	0.88	0.95
γ_0^c	0.0605	0.0364	0.0294	0.0137
γ_1^c	−0.0830	−0.0567	−0.0447	−0.0243
γ_2^c	0.0975	0.0423	0.0440	0.0179
γ_3^c	0.0625	0.0141	0.0213	0.0045
γ_4^c	0.0106	−0.0360	−0.0032	−0.0107
Q^c	1.57	0.97	0.75	0.38

TABLE 1. NOB effects with differing strengths are studied systematically by performing experiments under different conditions, E-I, E-II, E-III and E-IV. As shown in the table, each condition is characterized by a choice of fluid and lateral boundary along with key parameter values, including the cell depth d, the aspect ratio Γ, the pressure P, the critical temperature difference across the cell ΔT_c, the vertical diffusion time $t_v = d^2/\kappa$, the Prandtl number σ, and the coefficients γ_i^c used to calculate the Busse parameter Q^c at onset.

gaseous CO_2 in one experiment (E-II) with a paper boundary. The aspect ratio Γ is held nearly constant for all experiments. The onset Busse parameter Q^c is calculated from (1.4) with the coefficients γ_i^c evaluated at the onset of convection ($\epsilon = 0$). (The fluid properties necessary to calculate the coefficients γ_i in (1.5) for the range of experimental parameters are available at journals.cambridge.org/flm as supplementary material.) The experimental conditions E-I and E-IV represent, respectively, the largest and the smallest departures from OB convection at onset.

The NOB effects near onset can affect the critical Rayleigh number Ra_c if they are strong enough. In a recent study by Ahlers *et al.* (2009), the NOB corrections to $Ra_c = 1707.8$, i.e. $\delta Ra_c = Ra_c^{NOB} - Ra_c$, are computed numerically. The corrections are small in our experiments. For example, at onset $\delta Ra_c = 1.7$ in E-I and $\delta Ra_c \approx 0$ in E-IV (for calculations see (6.9) and table 6 in Ahlers *et al.* 2009). We perform experiments at different ranges of ϵ by increasing the temperature difference ΔT at a constant mean temperature $\bar{T}$ (measured at onset) between top and bottom plates. The correction to Ra_c used to estimate ϵ at larger ΔT is small even for the case where NOB effects are largest at onset, e.g. for $\epsilon = 0.8$ in E-I, the correction to Ra_c is 0.3 %.

Away from the onset ($\epsilon > 0$), the NOB effects become stronger. The ϵ dependence of NOB effects, especially in numerical simulations, is usually characterized by the coefficients (Madruga *et al.* 2006; Madruga & Riecke 2007*a*)

$$\gamma_i \cong \gamma_i^c(1 + \epsilon), \tag{2.1}$$

which is obtained by keeping only the leading-order temperature dependence in a Taylor expansion of all fluid properties. In experiments with real gases, (2.1) holds for order-one values of ϵ. For instance, at $\epsilon = 0.8$, the values of γ_i evaluated from real gas properties and the values of γ_i obtained via (2.1) agree with one another by a mean deviation of 0.8 % and 0.3 % for experiments E-I and E-II, respectively. Here σ evaluated at the top and bottom temperatures differs only slightly from σ evaluated at $\bar{T}$; this variation of σ over increasing ϵ can be estimated from $(1/\sigma)(d\sigma/d\epsilon)$, which

Run	Experiment	Reduced Rayleigh number	Busse parameter	$\bar{T}$ (°C)	$t_{obs}(t_h)$	N
R-I	E-I	$\epsilon = 0.8$	$Q = 2.80$	29.92	53	5000
R-II	E-II	$\epsilon = 0.8$	$Q = 1.75$	20.55	50	15 000
R-III	E-III	$\epsilon = 0.8$	$Q = 1.35$	27.51	208	5000
R-IV	E-IV	$\epsilon = 0.8$	$Q = 0.65$	25.85	130	5000
R-V	E-III	$1.0 \leqslant \epsilon \leqslant 2.7$	$1.50 \leqslant Q \leqslant 2.79$	27.51	10	5000
R-VI	E-IV	$1.0 \leqslant \epsilon \leqslant 3.0$	$0.73 \leqslant Q \leqslant 1.44$	25.85	10	5000

TABLE 2. Key conditions are shown for experimental runs R-I, R-II, R-III, R-IV, R-V and R-VI to probe NOB effects in SDC. Q is estimated from (1.4) with the fluid properties (see supplementary material) evaluated at ϵ values. The number of images N is acquired in experiments in observation times t_{obs} in units of the horizontal diffusion time t_h ($t_h = \Gamma^2 t_v$).

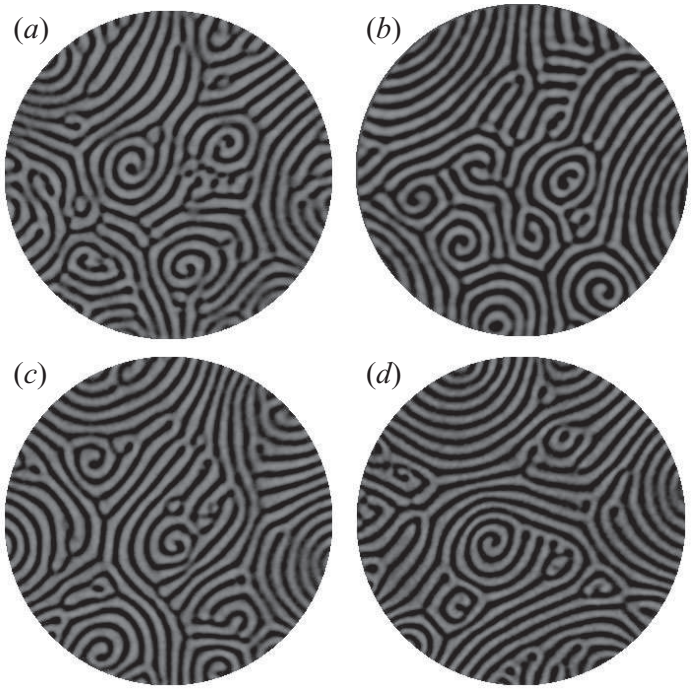

FIGURE 1. Shadowgraph patterns at fixed $\epsilon = 0.8$ and different values of Q illustrate that variations in NOB effects are indistinguishable by eye. The images are shown for experimental runs (*a*) R-I, (*b*) R-II, (*c*) R-III and (*d*) R-IV (table 2). Dark and bright regions in images represent hot and cold flows, respectively. Homology computations yield the following set of Betti numbers for these patterns $\{\beta_{0c}, \beta_{0h}, \beta_{1c}, \beta_{1h}\}$: (*a*), $\{54, 29, 1, 9\}$; (*b*), $\{42, 28, 3, 8\}$; (*c*), $\{43, 34, 0, 4\}$; (*d*), $\{43, 44, 4, 4\}$. How Betti numbers are computed from shadowgraph images of convection patterns can be found in detail with illustrations in Krishan *et al.* (2007).

is equal to 0.015, 0.040, 0.010 and 0.009 for E-I, E-II, E-III and E-IV, respectively, for $\epsilon \leqslant 3.0$.

The temperature difference ΔT is increased in each experiment from onset at a constant $\bar{T}$ to reach ϵ values for which SDC is fully developed. Shadowgraph image time series of spatio-temporally chaotic flow are acquired at a fixed frame rate for long observation time intervals, i.e. the intervals are large multiples of the horizontal diffusion time t_h ($t_h = \Gamma^2 t_v$, where t_v is the vertical diffusion time). Four different runs, indicated by R-I, R-II, R-III and R-IV, are performed at $\epsilon = 0.8$, as summarized in table 2. Sample images of patterns from these runs are shown in figure 1. Moreover, experimental runs R-V and R-VI are performed to probe the departure

from the OB convection at higher Rayleigh numbers ($\epsilon > 1$). In all experimental runs, the shadowgraph images are pre-processed for the analysis by first subtracting a background image taken below the onset from images and then by normalizing each image by the background to reduce non-uniformities due to the illumination.

3. Results

3.1. *Homology analysis*

Algebraic topology, in particular homology, provides a computable tool for characterizing global geometric properties of nonlinear objects. A package of computer programs (Kaczynski, Mischaikow & Mrozek 2004; CHomP 2010) has been developed to compute the homology groups of topological spaces in arbitrary dimensions. Given a topological space X of the type considered in this paper, the homology groups of interest take the form $H_k(X) = Z^{\beta_k(X)}$, $k = 0, 1$, where the non-negative integers $\beta_k(X)$ are referred to as the Betti numbers of X. Each $\beta_k(X)$ describes a unique topological property of X.

The shadowgraph patterns of figure 1 are used to define two distinct topological spaces of interest: the regions of cold and hot flows. The median value of intensity for all pixels in an image is used as a threshold value to form two distinct binary images that represent the locations of hot and cold flows. Any pixel value lower (higher) than the threshold value is defined to belong to the hot (cold) topological space X_h (X_c). The resulting binary images are used to obtain $\{\beta_{0c}, \beta_{0h}, \beta_{1c}, \beta_{1h}\}$, which provides a reduced topological description of the pattern (figure 1). In particular, β_{0c} (β_{0h}) counts the number of distinct connected cold (hot) components and β_{1c} (β_{1h}) counts the number of holes formed within X_c (X_h). Alternatively, β_{1c} (β_{1h}) counts the number of hot (cold) connected regions completely surrounded by cold (hot) flow. We note that the measurements of the Betti numbers are robust to variations in the choice of threshold value (Krishan *et al.* 2007).

Because of its combinatorial nature, there are no errors involved in computing the homology of a topological space defined in terms of pixels. Thus, the only possible error in the Betti number ascribed to the hot and cold regions arises from the approximation due to the pixelation of the image. Since the topological structures of these regions change with time, it is likely that errors do arise. Nevertheless, the results of Mischaikow & Wanner (2007) indicate that sufficiently high-resolution images lead to a high probability of correctly determining the Betti number.

Krishan *et al.* (2007) applied computational homology to convection patterns in RBC and suggested that the asymmetries revealed by Betti numbers are due to the NOB effects. They also showed that the strength of topological asymmetries increases with increasing bottom layer temperature while holding the top layer temperature constant in an experiment performed with CO_2. This paper explores the quantitative connection between the degree of the topological asymmetry and the measure Q in controlled RBC experiments.

We first focus on the time-averaged values of the Betti numbers $\{\langle\beta_{0c}\rangle, \langle\beta_{0h}\rangle, \langle\beta_{1c}\rangle, \langle\beta_{1h}\rangle\}$ calculated from the time series of binary images in experimental runs at $\epsilon = 0.8$. The distinction between cold and hot flows based on the mean Betti numbers becomes more substantial as Q increases, as seen in figure 2. The nearly equal number of components and holes points out the strong symmetry between cold and hot flows for the run R-IV with the weakest NOB effects; nevertheless, the asymmetry $\langle\beta_{0c}\rangle > \langle\beta_{0h}\rangle$, $\langle\beta_{1h}\rangle > \langle\beta_{1c}\rangle$ is significant for the run R-I, which indicates a strong breakdown of the OB approximation. The asymmetry is also

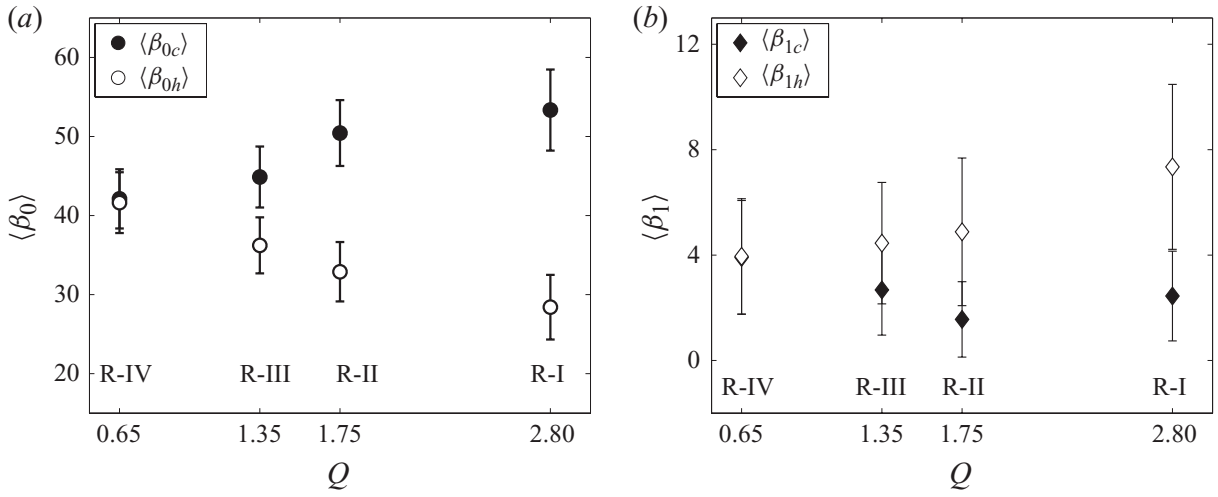

FIGURE 2. Topological asymmetries increase with the Busse parameter Q at constant ϵ. (*a*) The mean zeroth Betti numbers $\langle\beta_{0c}\rangle$ (filled circles) and $\langle\beta_{0h}\rangle$ (open circles); (*b*) the mean first Betti numbers $\langle\beta_{1c}\rangle$ (filled diamonds) and $\langle\beta_{1h}\rangle$ (open diamonds) are calculated from the time series of Betti numbers for the experimental runs (table 2) at $\epsilon = 0.8$. In computations, 5000 images are analysed for the runs R-I, R-III and R-IV, while 15 000 images are used in computations for the run R-II. The error bars are defined as the standard deviation of the Betti numbers obtained from the time series of shadowgraph images at a given ϵ.

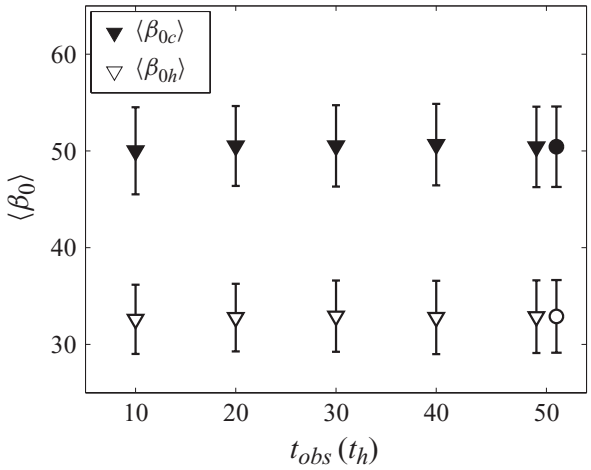

FIGURE 3. Temporal convergence of the mean zeroth Betti number in R-II. $\langle\beta_{0c}\rangle$ (filled triangles) and $\langle\beta_{0h}\rangle$ (open triangles) are shown as a function of observation time. Each data point corresponds to an average of Betti numbers from the analysis of 3000 images. The results for the original data of 15000 images in $50t_h$ (figure 2*a*) are shown by circles.

apparent for the run R-II, where a different type of convective fluid and physical boundary is used. These results suggest that the outputs of homology, especially the zeroth Betti number β_0, can be used to study the degree of departure from the OB convection.

The time averages of the Betti numbers are well defined for a wide range of observation time intervals (figure 3). We demonstrate the temporal convergence of the mean zeroth Betti number in time by truncating the time series of β_{0c} and β_{0h} with different sampling rates in R-II. As shown in figure 3, the results obtained by averaging the Betti numbers of the same size are nearly constant with increasing observation time.

It is known that shadowgraph visualization can introduce nonlinearities depending on visualization conditions; these nonlinearities may affect the accuracy of the

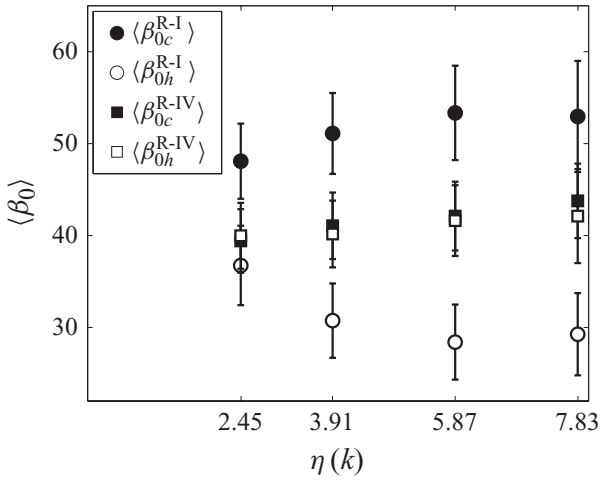

FIGURE 4. Robustness of the measurement of the mean zeroth Betti number with respect to wavenumber distribution. The zeroth Betti numbers, $\langle\beta_{0c}\rangle$ and $\langle\beta_{0h}\rangle$, computed for the images filtered with a two-dimensional Gaussian filter of variance η in units of k. Computations are performed for two data sets, R-I (circles) and R-IV (squares). Filters with $\eta(k=2.45)$ and $\eta(k=7.83)$ keep 59 % and 95 % of the total power, respectively. k is measured in units of d^{-1}.

measurement. Robustness of the measurements of Betti numbers has been shown with respect to different effective optical distances resulting in different strengths of the nonlinearities (Krishan *et al.* 2007). These nonlinearities may also introduce higher harmonics in the wavevector ($\boldsymbol{k}$) distribution, where the strength of the harmonics increases with ϵ. Here, we investigate how the measurements of Betti numbers depend on the $\boldsymbol{k}$-distribution (see § 3.2). For this purpose, a two-dimensional Gaussian filter is centred at $\boldsymbol{k}=0$ with a variance $\eta(k)$ and applied to the Fourier domain of the images to alter the distribution and to reduce the power in higher harmonics. Figure 4 demonstrates $\langle\beta_{0c}\rangle$ and $\langle\beta_{0h}\rangle$ computed for the images filtered with different $\eta(k)$. The weak asymmetry for weakly NOB flows (R-IV) and the strong asymmetry for strongly NOB flows (R-I) are clearly evident even for the filter with $\eta(k=2.45)$, which retains only 59 % of the total power in the original images. Computations performed with a Gaussian filter centred at the peak of the $\boldsymbol{k}$-distribution also yields similar results.

In order to demonstrate that the asymmetries, when they exist, extend throughout the cell, we performed computations in the subregions, which are obtained by sampling the images spatially with a circular window of increasing radii r centred at the centre of the convection cell. The zeroth Betti numbers are computed at each subregion. The scalings of $\langle\beta_{0c}\rangle$ and $\langle\beta_{0h}\rangle$, computed for many subregions for R-II and five subregions for R-IV, are displayed with increasing subregion area in figure 5(a). The circular regions for $r<5d$ are too small to extract information since only a few convection rolls (in binary representation) can fit such small regions. As soon as the subregion is large enough, the asymmetry is detected by Betti numbers. It is convenient to define an order parameter $\langle\Delta\beta_0\rangle=\langle\beta_{0c}-\beta_{0h}\rangle$ to examine the scaling of the asymmetry along the cell. As seen in figure 5(b), the asymmetry, $\langle\Delta\beta_0\rangle>0$, grows with the area; it is noticeable for subregions chosen as small as the half of the cell in R-II. On the other hand, the symmetry, $\langle\Delta\beta_0\rangle\approx 0$, is preserved along the cell in R-IV, i.e. the asymmetry between cold and hot flows is indistinguishable whether in a small region ($r=5d$) or in a large region that almost covers the entire cell ($r=30d$).

The more the system is driven away from the onset, the more NOB the fluid becomes as Q grows with the Rayleigh number. We analyse the data sets from R-V and R-VI described in table 2 to investigate the departure from the OB approximation at

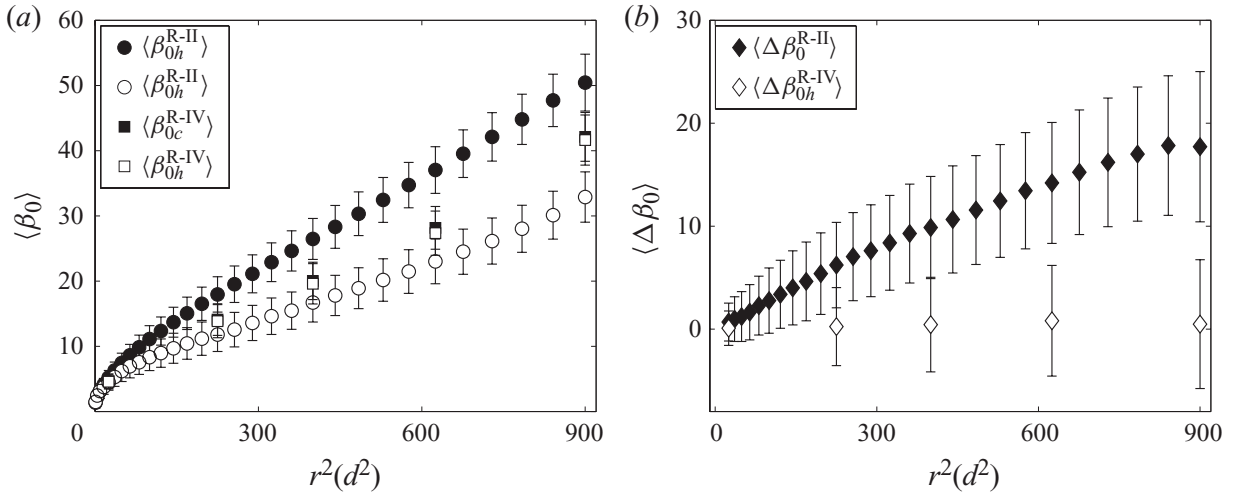

FIGURE 5. Scaling of the topological symmetry and asymmetry with system size. The zeroth mean Betti numbers are shown as a function of the area of circular subregions of radius r (r is in units of the cell depth d). (*a*) In run R-II ($Q = 1.75$) indicated by circles, $\langle\beta_{0c}\rangle$ and $\langle\beta_{0h}\rangle$ are obtained by analysing 15000 images in increasing size of subregions formed by an increment d in r. In R-IV ($Q = 0.65$) indicated by squares, 5000 images are used to calculate the zeroth Betti numbers for five subregions of different sizes ($r = 5d,\ 15d,\ 20d,\ 25d,\ 30d$). (*b*) The order parameter $\langle\Delta\beta_0\rangle = \langle\beta_{0c} - \beta_{0h}\rangle$ is shown as a function of the subregion area for R-II (closed symbols) and R-IV (open symbols).

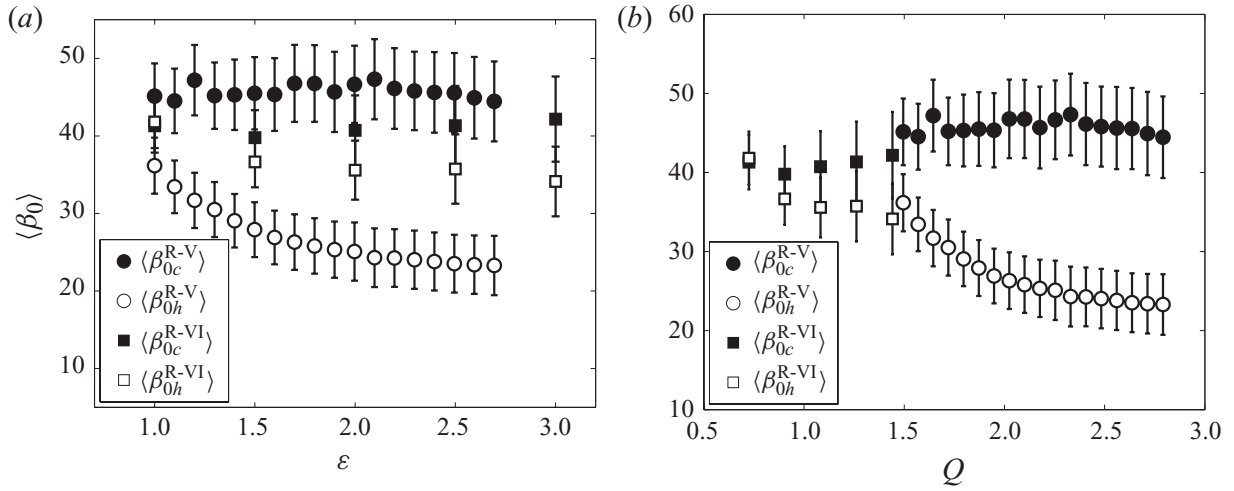

FIGURE 6. Topological asymmetries grow with the Rayleigh number. (*a*) $\langle\beta_{0c}\rangle$ (filled symbols) and $\langle\beta_{0h}\rangle$ (empty symbols) are shown as a function of ϵ for runs R-V (circles) and R-VI (squares). Each data point is obtained by averaging the Betti numbers from the analysis of 5000 images corresponding to an observation time of $10t_h$ at each ϵ. (*b*) The zeroth Betti numbers are shown as a function of Q estimated at the ϵ values in R-V and R-VI.

higher Rayleigh numbers ($1 \leqslant \epsilon$). Figure 6(*a*) exhibits $\langle\beta_{0c}\rangle$ and $\langle\beta_{0h}\rangle$ computed for 18 increasing ϵ values (with an increment of 0.1 in ϵ) in R-V, and for 5 increasing ϵ values (with an increment 0.5 in ϵ) in R-VI. The difference between $\langle\beta_{0c}\rangle$ and $\langle\beta_{0h}\rangle$ starts to become more substantial as ϵ increases for each run. The different runs exhibit a different dependence on ϵ; however, when plotted as a function of Q (figure 6*b*), a curve for $\langle\beta_{0c}\rangle$ and another curve for $\langle\beta_{0h}\rangle$ appear to describe the data from both runs.

Figure 6(*b*) suggests that the zeroth Betti number data from all experimental runs may be represented by a plot of the order parameter $\langle\Delta\beta_0\rangle$ as a function of Q (figure 7). The collapse of the data on a single curve suggests that the strength of the

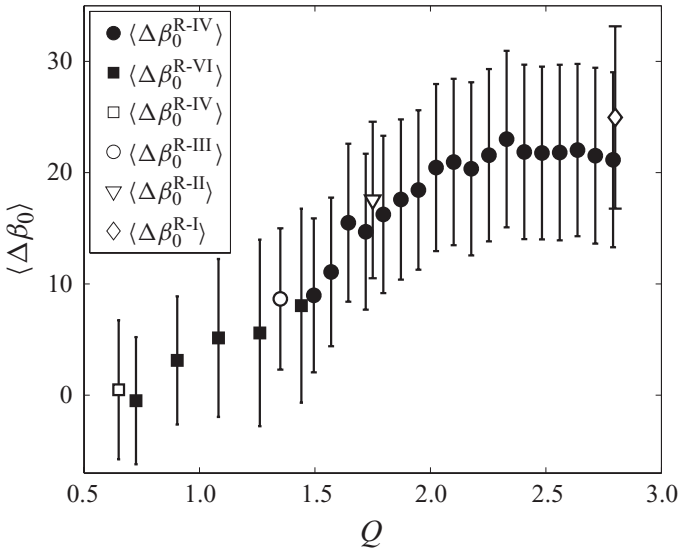

FIGURE 7. The zeroth Betti number data for *all* our experimental runs (table 2) are represented by a single graph of $\langle\Delta\beta_0\rangle = \langle\beta_{0c} - \beta_{0h}\rangle$ plotted solely as a function of the NOB parameter Q. Data are shown for experimental runs R-I (open diamond), R-II (open triangle), R-III (open circle), R-IV (open square), R-V (closed circles) and R-VI (closed squares).

topological asymmetry is solely dependent on NOB effects as characterized by Q. For a range of Q, $\langle\Delta\beta_0\rangle$ monotonically increases with Q. However, for Q sufficiently large (here, $Q > 2$), $\langle\Delta\beta_0\rangle$ is nearly constant at large Q; specifically, we find $\langle\beta_{0c}\rangle \approx 2\langle\beta_{0h}\rangle$ in R-V and R-I for $Q > 2$. Clearly, this result suggests that $\langle\Delta\beta_0\rangle$ does not distinguish flows with different Q when Q is sufficiently large. However, we do not know the physical origin of this 'saturation' of $\langle\Delta\beta_0\rangle$ for large Q; nor do we know whether this behaviour might be different for flow parameters not explored here (e.g. different Prandtl number and aspect ratio).

3.2. *Other analysis methods*

When a new technique for pattern analysis is introduced, it is sensible to examine the question whether more established methods could also be used to accomplish the same purpose. Here, we apply alternative characterization techniques to analyse the same convection pattern data. Although these techniques provide a variety of significant information about the global features of the patterns, as demonstrated next, they fail to identify the asymmetries that arise between cold and hot flows, even under the strong NOB effects.

The structure factor $S(\boldsymbol{k})$, the time average of the power (the square of the modulus) of the two-dimensional Fourier transform, is most often used to extract spatial information about the patterns (Morris *et al.* 1993, 1996; Hu, Ecke & Ahlers 1995). We perform an azimuthal average in wavevector ($\boldsymbol{k}$) space on each discrete Fourier transform of the image. The azimuthally and time-averaged $S(\boldsymbol{k})$ is obtained from the time series of images. The average wavenumber $\langle k\rangle$,

$$\langle k\rangle = \frac{\int |\boldsymbol{k}| S(\boldsymbol{k})\,\mathrm{d}^2\boldsymbol{k}}{\int S(\boldsymbol{k})\,\mathrm{d}^2\boldsymbol{k}} = \frac{\int_0^\infty k^2 S(k)\,\mathrm{d}k}{\int_0^\infty k S(k)\,\mathrm{d}k}, \tag{3.1}$$

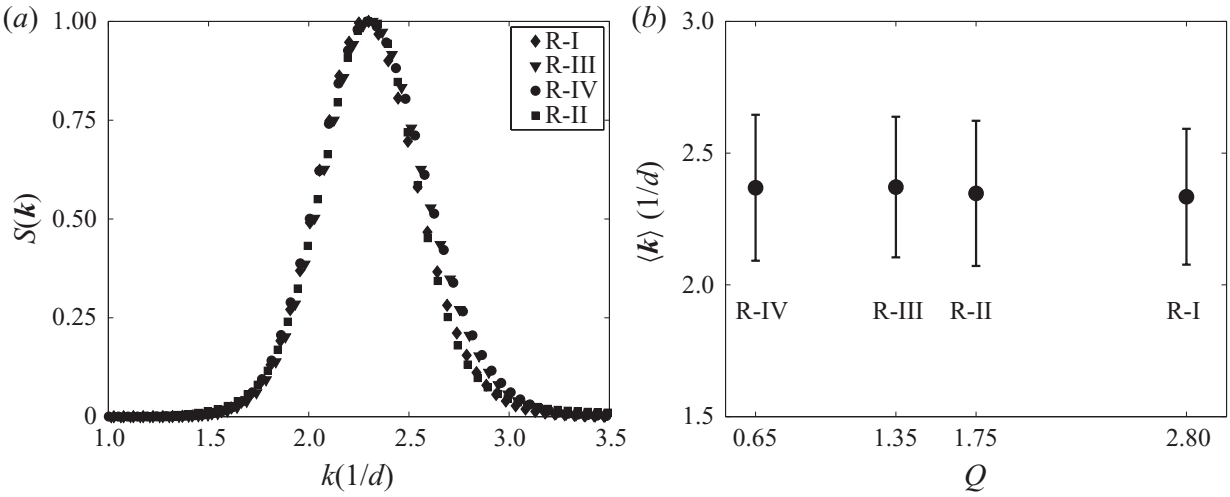

FIGURE 8. The analysis based on two-dimensional discrete Fourier transform produces nearly identical results for the patterns, on which NOB effects are varied. (*a*) The azimuthally and time-averaged structure factor $S(\boldsymbol{k})$ corresponding to the runs at $\epsilon = 0.8$. (*b*) The mean wavenumber $\langle k \rangle$ as a function of Q. The error bars in (*b*) represent one standard deviation which corresponds to the inverse of the correlation length ξ^{-1}.

and the correlation length ξ from the variance,

$$\xi^{-2} = \frac{\displaystyle\int_0^\infty (k - \langle k \rangle)^2 k S(k)\, \mathrm{d}k}{\displaystyle\int_0^\infty k S(k)\, \mathrm{d}k}, \tag{3.2}$$

are calculated from the distribution of $S(\boldsymbol{k})$ (Morris *et al.* 1993). $S(\boldsymbol{k})$ computed for the data sets at $\epsilon = 0.8$ is shown in figure 8(*a*). Figure 8(*b*) presents $\langle k \rangle$ as a function of Q, where the vertical extent is given by ξ^{-1}. The data produce nearly identical wavenumber distributions as Q is varied. In addition, the correlation area ($\propto \xi^2$) remains a constant percentage (nearly 1.5 %) of the total cell area for all cases. We note that $S(\boldsymbol{k})$ does not provide quantitative characterization between cold and hot flows since it produces identical results for complementary images as dark (bright) pixels are transformed into bright (dark) pixels.

Methods of characterizing pattern textures have also been used previously to quantify important features of flow patterns (Heutmaker & Gollub 1987; Hu *et al.* 1995); however, this approach fails to detect non-Boussinesq effects. In our study, the texture of a cold (hot) flow pattern is obtained from a skeleton-line representation corresponding to maximum (minimum) intensity regions in the image of a convection pattern. On these textures, we calculate the average roll radius of the curvature $\langle \mathscr{R} \rangle = \langle 2/|\nabla \cdot \boldsymbol{n}| \rangle$ (a measure of how much a roll bends), the average roll length $\langle L \rangle$, and the average roll obliqueness at the sidewall $\langle \theta \rangle = \langle \cos^{-1}(|\boldsymbol{s} \cdot \boldsymbol{n}|) \rangle$, where $\boldsymbol{n}$ is the unit normal vector parallel to the local wavevector and $\boldsymbol{s}$ is the sidewall normal vector. (A detailed discussion of texture analysis methods can be found elsewhere; Heutmaker & Gollub 1987; Hu *et al.* 1995.) In figure 9, we see that none of these measures of texture exhibit dependence on the strength of non-Boussinesq effects as characterized by Q. In particular, the values of $\langle \mathscr{R} \rangle$, calculated both for the full circular region of the cell and a smaller circular region ($r = 20d$), remain quite close to each other even as Q is increased by a factor of 4 (figure 9*a*) with no observable distinction between cold and hot flow patterns ($\langle \mathscr{R}_c \rangle \approx \langle \mathscr{R}_h \rangle$). Similarly, we find that $\langle L_c \rangle \approx \langle L_h \rangle$ (figure 9*b*) and $\langle \theta \rangle$ is constant (figure 9*c*) over a wide range of Q. In contrast, we do find

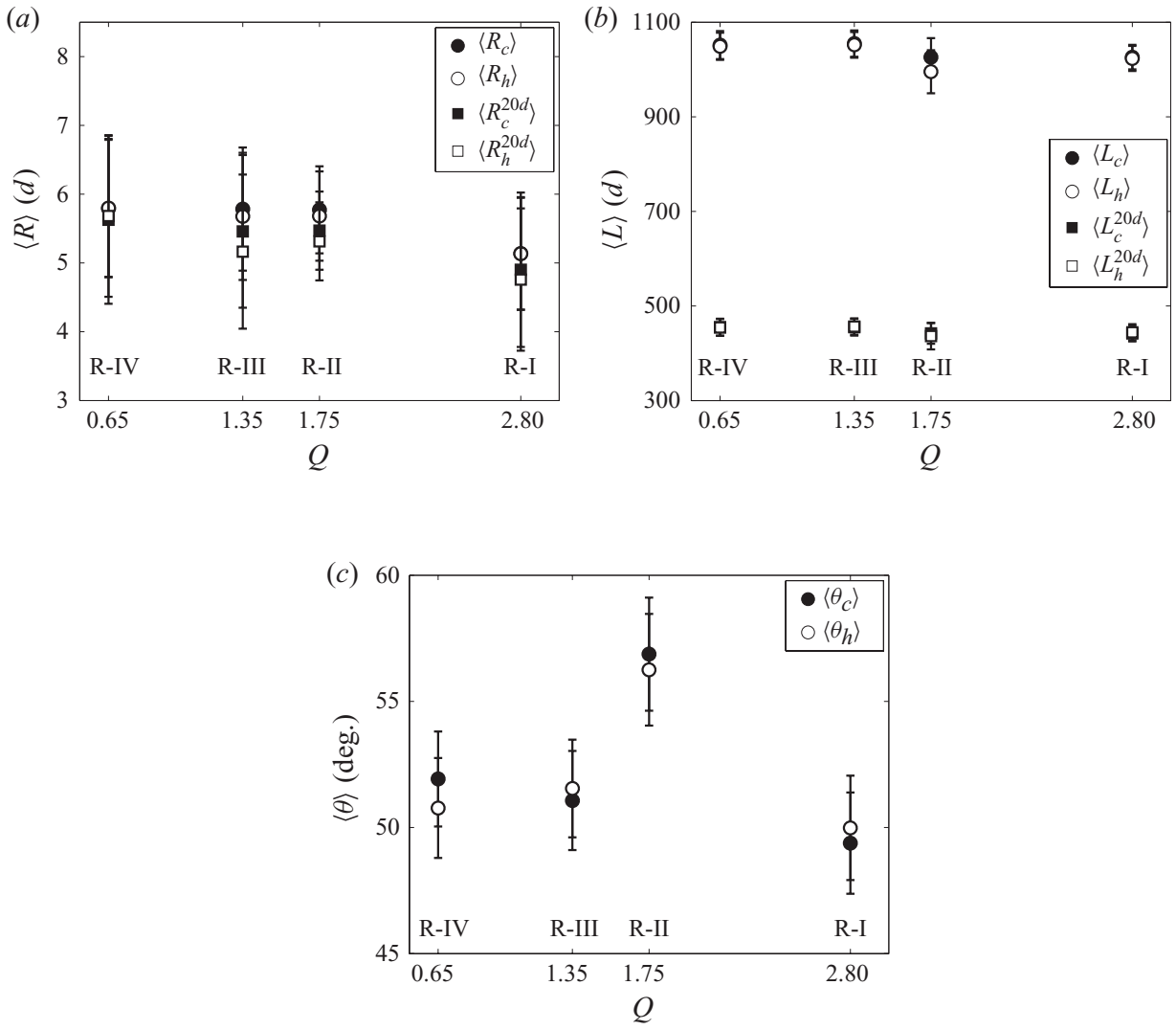

FIGURE 9. Measures calculated from the texture of the patterns for the runs at $\epsilon = 0.8$ show no distinction between cold and hot flow patterns as a function of Q. The number of images used at each point is given in table 2. The subscripts c and h indicate the obtained quantities for cold and hot flows, respectively. (a) The time-averaged radius of curvatures $\langle \mathscr{R} \rangle$ calculated for full system size and a circular region of radius $r = 20d$ inside the cell. (b) The time-averaged roll length $\langle L \rangle$ shown for full system size and a circular region of radius $r = 20d$. (c) The time-averaged angle of obliqueness $\langle \theta \rangle$.

that texture analysis can detect differences in sidewall forcing of convective flows. In the case with sidewalls whose thermal conductivity matches the fluid (no forcing), rolls terminate perpendicular to the walls ($\theta = 90^\circ$). However, in typical experiments, some sidewall forcing arises due to the mismatch in the thermal conductivity between the sidewall and the fluid that induces a horizontal temperature gradient near the wall. This mismatch induces forcing that tends to push the rolls to be more parallel to the sidewall (Hu, Ecke & Ahlers 1993; Xi & Gunton 1995). This effect can be seen in figure 9(c); convection rolls are more parallel to sidewalls made of plastic (larger forcing due a larger conductivity mismatch) than rolls in the presence of paper sidewalls (which have a smaller conductivity mismatch).

4. Discussion and conclusion

Our results are consistent with well-known symmetries/asymmetries of convective flows that arise at onset (de Bruyn *et al.* 1996). Under Boussinesq conditions, gases

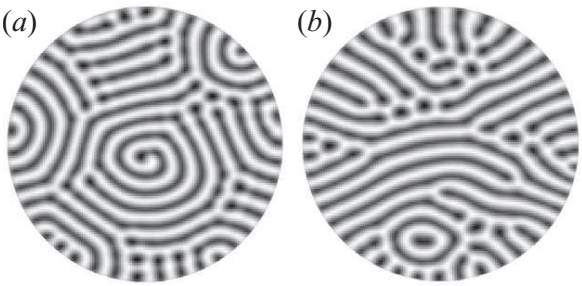

FIGURE 10. Contrary to convection in gases, patterns in liquids with negative Q have the asymmetry $\beta_{0h} > \beta_{0c},\ \beta_{1c} > \beta_{1h}$. For instance, temperature fields from an NOB simulation in a circular cell of water are shown at (*a*) $\epsilon = 0.6$ and (*b*) $\epsilon = 1.0$, after Madruga & Riecke (2007*b*). All coefficients, $\gamma_0^c = 0.0036$, $\gamma_1^c = 0.2122$, $\gamma_2^c = -0.2725$, $\gamma_3^c = 0.0352$ and $\gamma_4^c = -0.0013$ corresponding to $Q^c = -1.84$, are retained. The diameter of the cell is equal to 16 times the pattern wavelength at onset. Computations yield the following set of Betti numbers $\{\beta_{0c}, \beta_{0h}, \beta_{1c}, \beta_{1h}\}$: (*a*), $\{11, 37, 6, 0\}$; (*b*), $\{5, 48, 10, 1\}$.

exhibit straight-roll convection via a supercritical bifurcation. Homology simply yields $\beta_{0c} = \beta_{0h} = N$ and $\beta_{1h} = \beta_{1c} = 0$ for N straight rolls in a pattern (without sidewall forcing at onset). In the NOB case, the flow exhibits a transcritical bifurcation at onset where gases with positive Q (as in our experiments) display g-hexagons with (cold) downflow in the centre (see sample patterns in Bodenschatz *et al.* 1991). Homology returns $\beta_{0c} = M > \beta_{0h} = 1$ and $\beta_{1h} = M > \beta_{1c} = 1$ for a pattern containing M g-hexagonal cells; in other words, the qualitative result of NOB effects leading to $\beta_{0c} > \beta_{0h},\ \beta_{1h} > \beta_{1c}$ patterns at onset is consistent with the interpretation that NOB effects are responsible for our observations of $\beta_{0c} > \beta_{0h}$ well above onset. We note that hexagons are not observed over the parameter range examined in our study; nevertheless, Madruga & Riecke (2007*a*) have suggested that resonant triad interactions may be acting far from onset in a similar manner as near-convective onset to enhance the cellular character of the flow. A further test of this consistency can be found by examining the case of NOB convection in liquids, where Q is typically negative and l-hexagons with hot upflow in the centre are observed at onset (see a sample pattern in Ciliberto, Pampaloni & Peréz-García 1988). To examine the behaviour of Betti numbers in liquids well above onset, we performed an analysis of the homology of temperature field images from numerical simulations of NOB convection in water reported in Madruga & Riecke (2007*b*) and reproduced in figure 10. We find $\beta_{0h} > \beta_{0c},\ \beta_{1c} > \beta_{1h}$, i.e. for NOB flows in liquids, the Betti number asymmetry far from onset is consistent with the Betti number asymmetry for flows near onset.

Our method of characterizing NOB effects depends upon obtaining *averaged* homological quantities that are representative of the flow. Typically, the wide variety of patterns that could be observed at fixed parameter values (ϵ and Q) will correspond to differing topologies, as characterized by different values of Betti numbers. For the flows studied here, we use time-averaging to obtain representative averaged Betti numbers $\langle\beta_{0c}\rangle$, $\langle\beta_{0h}\rangle$, $\langle\beta_{1h}\rangle$, $\langle\beta_{1c}\rangle$; in essence, we rely on the time dependence of the flows' topology to sample ergotically the Betti numbers that are characteristic of (almost) all flows at fixed ϵ and Q. Time-averaging may miss contributions from patterns that lie in different basins of attractions; for example, the averaged Betti numbers we report here do not account for stable patterns of ideal straight rolls that can be observed in the range of ϵ explored in this study (Cakmur *et al.* 1997). We believe that neglecting the impact of these time-independent roll patterns on $\langle\beta_{0c}\rangle$, $\langle\beta_{0h}\rangle$,

$\langle\beta_{1h}\rangle$, $\langle\beta_{1c}\rangle$ is justified because these patterns can only be accessed by means of very special initial conditions (Cakmur *et al.* 1997); almost all initial conditions lead to the time-dependent spatio-temporal patterns examined in our work. However, for values of ϵ smaller than those examined here, time-independent patterns commonly arise at each value of ϵ. In this regime, time-averaging will fail; however, other approaches may be used to obtain $\langle\beta_{0c}\rangle$, $\langle\beta_{0h}\rangle$, $\langle\beta_{1h}\rangle$ and $\langle\beta_{1c}\rangle$. Representative patterns might be obtained by performing experiments that begin from a wide variety of different initial conditions (say, by use of external actuation (Semwogerere & Schatz 2004) or rapid quenching from a larger value of ϵ). Such patterns would typically contain defects of differing number, variety and distribution; thus, such patterns would typically exhibit differing Betti numbers. We speculate that by averaging Betti numbers over a suitable number of such patterns, it may still be possible to describe NOB effects using $\langle\beta_{0c}\rangle$, $\langle\beta_{0h}\rangle$, $\langle\beta_{1h}\rangle$, $\langle\beta_{1c}\rangle$ perhaps to very near the (subcritical) onset of convective flow. In this regard, future experiments to examine this issue would be of interest.

We expect our results to hold for the analysis of measurements other than the shadowgraph data discussed here. In earlier work, we demonstrated qualitatively that homology reveals Betti number asymmetries in both temperature and vertical velocity fields computed from numerical simulations of NOB convection (Krishan *et al.* 2007). Moreover, we found that the time-averaged Betti numbers extracted from time series of images in OB simulations showed little distinction between hot and cold flows in both temperature and velocity fields. It would be interesting to see if the NOB order parameter proposed here $\langle\Delta\beta_0\rangle$ exhibits the same behaviour as a function of Q (along the lines shown in figure 7), independent of the data field used to extract the homology. In this regard, experiments carried out in parallel with numerical simulations at the same parameter values would prove to be most useful; such studies could also help develop a theoretical understanding of how the results of the (present) empirical homology analysis can be directly related to physical mechanisms in the fluid flow.

Our results suggest that homology may be a useful tool to detect and quantify symmetry breaking due to other mechanisms or in other pattern forming complex systems. Although we find that homology is a quantitatively useful tool to investigate the breaking of a particular symmetry (reflection symmetry) due to a particular mechanism (the breakdown of the Oberbeck–Boussinesq approximation), we do not claim that measures of homology are only to be used or are only useful to detect NOB symmetry breaking. It is quite possible, for example, that homology might be used to quantify the breaking of rotational and reflection symmetry in Rayleigh–Bénard convection due to a completely different mechanism: the rotation of the flow about a vertical axis. In fact, it would be very interesting to examine flows where multiple causes of symmetry breaking are simultaneously present (e.g. NOB effects and rotation in Rayleigh–Bénard convection) to see if homological measures might be constructed to distinguish the impact of these different mechanisms. Likewise, it would be of interest to examine whether homology may offer new insights in pattern-forming complex systems other than Rayleigh–Bénard convection (e.g. convection in a nematic liquid crystal with a magnetic field) that also exhibit symmetry breaking.

H.K. thanks A. Perkins for his helpful comments on this work. We also thank G. Ahlers for the suggestion to analyse the homology of NOB convection in liquids far from onset. This work is supported by the Department of Energy under grant 97891.

K.M. is partially supported by AFOSR, DARPA, NSF-DMS0915019 and NSF-CDI 0835621.

Supplementary data are available at journals.cambridge.org/flm.

REFERENCES

Ahlers, G., Dressel, B., Oh, J. & Pesch, W. 2009 Strong non-Boussinesq effects near the onset of convection in a fluid near its critical point. *J. Fluid Mech.* **642**, 15–48.

Bodenschatz, E., de Bruyn, J. R., Ahlers, G. & Cannell, D. S. 1991 Transition between patterns in thermal convection. *Phys. Rev. Lett.* **67**, 3078–3081.

Bodenschatz, E., Pesch, W. & Ahlers, G. 2000 Recent developments in Rayleigh–Bénard convection. *Annu. Rev. Fluid Mech.* **32**, 709–778.

Boussinesq, J. 1903 *Théorie Analytique de la Chaleur*, vol. 2. Gauthier-Villars.

de Bruyn, J. R., Bodenschatz, E., Morris, S. W., Trainoff, S. P., Hu, Y., Cannell, D. S. & Ahlers, G. 1996 Apparatus for the study of Rayleigh–Bénard convection in gases under pressure. *Rev. Sci. Instrum.* **67**, 2043–2067.

Busse, F. H. 1967 The stability of finite amplitude cellular convection and its relation to an extremum principle. *J. Fluid Mech.* **30**, 625–649.

Cakmur, R. V., Egolf, D. A., Plapp, B. B. & Bodenschatz, E. 1997 Bistability and competition of spatiotemporal chaotic and fixed point attractors in Rayleigh–Bénard convection. *Phys. Rev. Lett.* **79**, 1853–1856.

CHomP 2010 *Computational Homology Project*. Available at: http://chomp.rutgers.edu.

Ciliberto, S., Pampaloni, E. & Peréz-García, C. 1988 Competition between different symmetries in convective patterns. *Phys. Rev. Lett.* **61**, 1198–1201.

Getling, A. V. 1998 *Rayleigh–Bénard Convection: Structures and Dynamics*. World Scientific.

Heutmaker, M. S. & Gollub, J. P. 1987 Wave-vector field of convective flow patterns. *Phys. Rev.* A **35**, 242–260.

Hu, Y., Ecke, R. & Ahlers, G. 1993 Convection near threshold for Prandtl numbers near 1. *Phys. Rev.* E **48**, 4399–4413.

Hu, Y., Ecke, R. E. & Ahlers, G. 1995 Convection for Prandtl numbers near 1: Dynamics of textured patterns. *Phys. Rev.* E **51**, 3263–3279.

Kaczynski, T., Mischaikow, K. & Mrozek, M. 2004 *Computational Homology*. Springer.

Krishan, K., Kurtuldu, H., Schatz, M. F., Madruga, S., Gameiro, M. & Mischaikow, K. 2007 Homology and symmetry breaking in Rayleigh–Bénard convection. *Phys. Fluids* **19**, 117105.

Madruga, S. & Riecke, H. 2007*a* Hexagons and spiral defect chaos in non-Boussinesq convection at low Prandtl numbers. *Phys. Rev.* E **75**, 026210.

Madruga, S. & Riecke, H. 2007*b* Reentrant and whirling hexagons in non-Boussinesq convection. *Eur. Phys. J. Special Topics* **146**, 279–290.

Madruga, S., Riecke, H. & Pesch, W. 2006 Re-entrant hexagons in non-Boussinesq convection. *J. Fluid Mech.* **548**, 341–360.

Mischaikow, K. & Wanner, T. 2007 Probabilistic validation of homology computations for nodal domains. *Ann. Appl. Prob.* **17**, 980–1018.

Morris, S. W., Bodenschatz, E., Cannell, D. S. & Ahlers, G. 1993 Spiral defect chaos in large aspect ratio Rayleigh–Bénard convection. *Phys. Rev. Lett.* **71**, 2026–2029.

Morris, S. W., Bodenschatz, E., Cannell, D. S. & Ahlers, G. 1996 The spatio-temporal structure of spiral-defect chaos. *Physica* D **97**, 164–179.

Niemela, J. & Sreenivasen, K. R. 2003 Confined turbulent convection. *J. Fluid Mech.* **481**, 355–384.

Oberbeck, A. 1879 Über die Wärmeleitung der Flüssigkeiten bei der Berücksichtigung der Strömungen infolge von Temperaturdifferenzen. *Ann. Phys. Chem.* **7**, 271–292.

Schluter, A., Lortz, D. & Busse, F. 1965 On the stability of steady finite amplitude convection. *J. Fluid Mech.* **23**, 129–144.

Semwogerere, D. & Schatz, M. F. 2004 Secondary instabilities of hexagonal patterns in a Bénard–Marangoni convection experiment. *Phys. Rev. Lett.* **93**, 124502.

Xi, H. & Gunton, J. D. 1995 Spatiotemporal chaos in a model of Rayleigh–Bénard convection. *Phys. Rev.* E **52**, 4963–4975.